Langmuir
ARTICLE
pubs.acs.org/Langmuir

Interfacial Transport of Evaporating Water Confined in Nanopores

Shankar Narayanan,[†] Andrei G. Fedorov,*[,†,‡] and Yogendra K. Joshi[†]

[†]George W. Woodruff School of Mechanical Engineering
[‡]Parker H. Petit Institute of Bioengineering and Biosciences, Georgia Institute of Technology, Atlanta, Georgia 30332, United States

Supporting Information

ABSTRACT: A semianalytical, continuum analysis of evaporation of water confined in a cylindrical nanopore is presented, wherein the combined effect of electrostatic interaction and van der Waals forces is taken into account. The equations governing fluid flow and heat transfer between liquid and vapor phases are partially integrated analytically, to yield a set of ordinary differential equations, which are solved numerically to determine the flow characteristics and effect on the resulting shape and rate of evaporation from the liquid−vapor interface. The analysis identifies three important parameters that significantly affect the overall performance of the system, namely, the capillary radius, pore-wall temperature, and the degree of saturation of vapor phase. The extension of meniscus is found to be prominent for smaller nanoscale capillaries, in turn yielding a greater net rate of evaporation per unit pore area. The effects of temperature and ambient vapor pressure on net rate of evaporation are shown to be analogous. An increase in pore-wall temperature, which enhances saturation pressure, or a decrease in the ambient vapor pressure result in enhancing the net potential for evaporation and increasing the curvature of the interface.

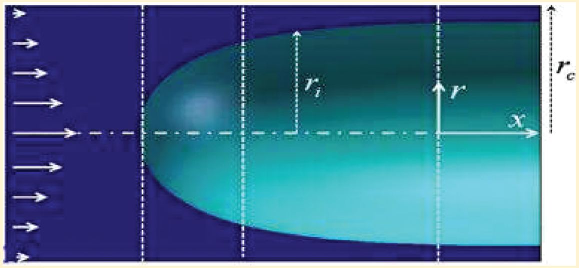

1. INTRODUCTION

A detailed understanding of wetting characteristics of liquids on plain or structured solid surfaces and their effect on phase change are required for many applications. In order to analyze wetting and interphase transport, it is essential to identify all relevant factors affecting contact line dynamics. Capillarity alone has been extensively studied for interpreting the wetting phenomenon. Its relation to the chemical constitution of both solid and liquid was used to explain the extent of spreading and the equilibrium contact angle during partial wetting.[1] However, as the length scale decreases below 1 μm, long-range interactions such as van der Waals forces can also play an important role, in addition to surface tension, to define the interface shape and, in turn, the rates of mass and heat transfer due to phase change at the interface. The three forces due to dipole induction, molecular orientation, and dispersion, which contribute toward the long-range interaction between two molecules, are collectively known as the van der Waals force. Among the constituent forces, dispersion is always present between molecules and is generally dominant, as compared to the dipole-dependent induction (Debye interactions) and orientation forces (Keesom interactions).[2]

An aspect of van der Waals force which is less prominently addressed in the existing literature for analysis of interfacial transport is the retardation effect. The dispersion interactions between surfaces decay rapidly at longer separations due to attenuation of electromagnetic coupling. For very short and long distances, a well-known asymptotic relation for disjoining pressure is given by $\Pi_d = -A_0/6\pi\delta^3$ and $\Pi_d = -B/\delta^4$, respectively, where A_0 is the nonretarded Hamaker's constant and B is the retarded dispersion constant,[3] which is applicable beyond the crossover length. This length is roughly related to the characteristic ultraviolet radiation absorption wavelength of the medium and is generally on the order of 800 Å.[1] While dispersion interactions are most significant in determining the disjoining pressure in the case of nonpolar liquids, electrostatic interaction between molecules cannot be neglected when a polar solvent is utilized. The presence of both dispersion and electrostatic interaction between two interacting mediums is addressed by the DLVO (Derjaguin−Landau−Verwey−Overbeek) theory.[4,5]

While DLVO can quantitatively describe electrostatic contribution toward surface forces in thin liquid films, it is now understood that additional interactions can exist which are "non-DLVO" in nature. From experimental observations, prior studies have estimated the effect of structural interactions in thin liquid films due to the forces other than van der Waals and DLVO interactions.[6−9] The structural component of disjoining pressure arises when interphase boundary layers, whose structure is different from that of the bulk liquid, overlap. Supported by experimental measurements, the structural component of disjoining pressure was found to decay exponentially with distance.[8] However, with dissolved ions in water, these additional forces still fail to explain the behavior of many colloidal systems. The concept of short-range hydration forces was then introduced to relate theory to experiments based on interaction of mica surface

Received: May 13, 2011
Revised: July 12, 2011
Published: July 13, 2011

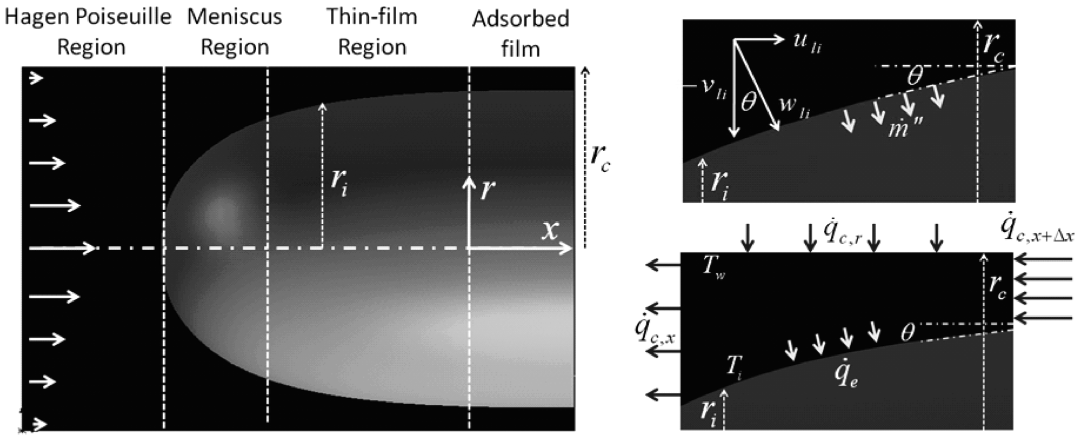

Figure 1. (a) Classification of the extended meniscus during evaporation. (b) Schematic for evaluation of normal interfacial velocity and illustration of various boundary heat fluxes.

with electrolyte solutions,[10] but this concept has been met with some skepticism,[11] and is still amidst validation. Yet, there are more recent concepts based on additional interaction modes, such as image charge forces, steric interactions, and hydrophobic forces with an aim to fully explain experimental observations.

Given the uncertainty in establishing and estimating the universally applicable force interactions, a comprehensive investigation of interfacial transport in water films is not only challenging, but currently incomplete. Therefore, our aim in this work is to carry out a simplified analysis to identify the prominence of different interactions for sustaining flow, mass and energy transport in evaporating liquid film confined within a nanoscale capillary and to gain a mechanistic understanding of the process physics. Evaporation of simple, nonpolar wetting liquids has been reported to elucidate effects arising due to van der Waals interactions, in addition to capillarity. In this regard, it is noteworthy to acknowledge the contribution of Wayner and co-workers in both theoretical developments and experimental validation.[12−14] Additionally, experimental studies[15−18] and computational analysis[19,20] of thermocapillary convection and velocity slip in channels during phase-change[20] are of relevance to the problem analyzed in this work.

In the analysis of phase-change of fluids in confined spaces, the rate of evaporation at the free surface needs to be modified from the commonly used expression given by Schrage.[21] That is, the change in equilibrium vapor pressure over a capillary meniscus, as compared to a "flat" interface, has to be accounted for using the Kelvin equation,[22] modified to include the effect of an adsorbed liquid film and presence of disjoining pressure.[23−25] Using interferometry, it has been shown that the predictions from the modified Kelvin equation match well with experimental measurements for capillary radii as small as several nanometers.[24]

Interfacial transport of nonpolar liquids is now well understood for evaporation in simple geometries like microchannels and cylindrical tubes.[12,13,15,16,19,20,26,27] However, the underlying solid−liquid−vapor interactions in previous studies were limited to dispersion and capillarity; the effect of electrostatic interactions, which are of much longer range, becomes important in the case of nanoconfined liquids and is analyzed in the current study.

2. ANALYSIS OF FLOW AND HEAT TRANSFER

The following mathematical model of fluid flow and heat transfer describes the interfacial transport of an evaporating meniscus inside a cylindrical pore. The cylindrical pore is assumed to be open-ended and exposed to atmospheric condition, which is a commonly encountered arrangement in practical applications of membrane-based phase-change processes. As a result, the interface is assumed to be surrounded by a gas phase comprising an air−vapor mixture at atmospheric pressure. The formulation presented herein includes the effects of capillary and disjoining pressures and also compares their importance relative to thermocapillary stresses (Marangoni effect) at different operating conditions.

At steady state, the shape of an evaporating interface inside a channel or pore is often broadly divided into three regions, as shown in Figure 1: (1) a thin adsorbed film in equilibrium with gaseous phase forms the leading edge of the liquid−vapor interface; (2) an adjacent thin-film region, which is significantly influenced by the disjoining pressure; and (3) the meniscus region where capillary pressure is a dominant force. Beyond the meniscus region, the flow can be considered fully developed, laminar, and well described by the Hagen−Poiseuille equation. In this analysis, the origin of the cylindrical coordinate system is located at the junction of the evaporating thin-film region and the adsorbed film, as shown in Figure 1. Numerical integration of governing equations is carried out with respect to the axial coordinate, x, to compute other flow variables for $x \leq 0$. The position of the interface is denoted by $r_i(x)$.

The model assumes a steady, axisymmetric, incompressible flow. Furthermore, the hydrostatic pressure and radial pressure gradient is neglected as compared to the dominant capillary, disjoining pressure, and axial pressure gradients. With these assumptions, the axial component of momentum balance for liquid flow is given by

$$-\frac{\mathrm{d}p_{li}}{\mathrm{d}x} + \frac{\mu_l}{r}\frac{\partial}{\partial r}\left(r\frac{\partial u_l}{\partial r}\right) = 0 \tag{1}$$

The boundary conditions for fluid flow are the no-slip at the walls, $u = 0$ at $r = r_c$, and thermocapillary stress balance at the interface, $-\mu_l(\partial u)/(\partial r) = (\partial\sigma)/(\partial x)$ at $r = r_i$.[27] The solution to the differential eq 1 with these boundary conditions is therefore given by

$$u_l = \left(-\frac{1}{4\mu_l}\frac{\mathrm{d}p_{li}}{\mathrm{d}x}\right)\left(r_c^2 - r^2 + 2r_i^2 \ln\frac{r}{r_c}\right) - \frac{r_i}{\mu_l}\frac{\partial\sigma}{\partial x}\ln\frac{r}{r_c} \tag{2}$$

The mass flow rate at any axial position can be obtained by integration, $\int \rho_l u_l (2\pi r)\,\mathrm{d}r$ between $r = r_i$ and $r = r_c$ to yield

$$\dot{m} = \frac{\pi\rho_l}{8\mu_l}\left(-\frac{\mathrm{d}p_{li}}{\mathrm{d}x}\right)\left[(r_c^2 - r_i^2)(r_c^2 - 3r_i^2) - 4r_i^4 \ln\frac{r_i}{r_c}\right] + \frac{\pi\rho_l}{8\mu_l}\left(\frac{\mathrm{d}\sigma}{\mathrm{d}T}\right)\left(\frac{\mathrm{d}T_{li}}{\mathrm{d}x}\right)\left[4r_i(r_c^2 - r_i^2) + 8r_i^3 \ln\frac{r_i}{r_c}\right] \quad (3)$$

The change in mass flow rate of the liquid along the axial position due to evaporation at the interface can be calculated in terms of the local mass flux. At any interfacial location, the mass flux is given by evaporation kinetics[21]

$$\dot{m}'' = \frac{2\hat{\sigma}}{2-\hat{\sigma}}\left(\frac{M}{2\pi R}\right)^{1/2}\left(\frac{p_{vi}}{T_{li}^{1/2}} - \frac{p_v}{T_v^{1/2}}\right) \quad (4)$$

where p_{vi} is the equilibrium vapor pressure, and p_v is the partial pressure of the vapor in the gas phase, which is a mixture of air and vapor at temperature T_v surrounding the interface. In order to relate mass flux to the velocity of liquid phase, the mass continuity equation, $\partial u_l/\partial x + (1/r)\partial(rv_l)/\partial r = 0$ is integrated between $r = r_i$ and $r = r_c$.

$$r_i v_{li} = \frac{\mathrm{d}}{\mathrm{d}x}\int_{r_i}^{r_c} r u_l\,\mathrm{d}r + r_i u_{li}\frac{\mathrm{d}r_i}{\mathrm{d}x} \quad (5)$$

Equation 5 assumes that $v_l = 0$ at $r = r_c$. Also, since the interface position r_i is a function of the axial variable, the Leibniz integral rule is used to obtain the expression at the right-hand side of eq 5. This equation is transformed in terms of mass flow rate to obtain

$$v_{li} = \frac{1}{2\pi\rho_l r_i}\frac{\mathrm{d}\dot{m}}{\mathrm{d}x} + u_{li}\frac{\mathrm{d}r_i}{\mathrm{d}x} \quad (6)$$

The interfacial velocity of liquid directed normal to the interface $w_{li} = \dot{m}''/\rho_l$ can be evaluated in terms of the velocity components and the slope of the interface $\theta = \tan^{-1}(\mathrm{d}r_i/\mathrm{d}x)$ as illustrated in the Figure 1b and is given by the following equation:

$$w_{li} = u_{li}\sin\theta - v_{li}\cos\theta \quad (7)$$

Using eqs 6 and 7, the mass flow rate at any axial location can be related to the rate of evaporation at the interface given by eq 4. The temperature discontinuity at the interface $(T_{li} - T_v)$ using kinetic theory is given by $-0.45(T_v/2R)^{1/2}u_v$,[28] where u_v represents the characteristic vapor speed during evaporation. By utilizing $\dot{m}''/\rho_v$ as an appropriate scale for u_v, the temperature jump is ~5 °C for a conservatively large approximation for $\dot{m}''$ of ~5 kg/m^{2}s. In this case, the assumption of thermal equilibrium would then introduce an error less than ~5% even for a high humidity (95% or $p_v/p_{vi} = 0.95$) ambient environment. Therefore, to simplify the analysis, the discontinuity in temperature at the interface between the liquid and gas phase is neglected by assuming local thermal equilibrium or $T_v = T_{li}$.[27]

$$-\frac{\cos\theta}{2\pi r_i}\frac{\mathrm{d}\dot{m}}{\mathrm{d}x} = \frac{2\hat{\sigma}}{2-\hat{\sigma}}\left(\frac{M}{2\pi R T_{li}}\right)^{1/2}(p_{vi} - p_v) \quad (8)$$

Equation 3 relates mass flow rate to two unknown variables, namely, the pressure and temperature gradients. The pressure distribution in the liquid phase can be obtained using balance of normal stress at the interface, while the interfacial temperature distribution is obtained using energy conservation.

Although the pressure in liquid phase varies along the interface, the total pressure of the gas phase consisting of air and evaporated vapor mixture can be assumed constant and equal to atmospheric pressure p_{atm}. This assumption is based on the evaluation of Knudsen number, $\mathrm{Kn} = M/(\sqrt{8\pi d^2}\rho_v N_A r_c)$for the transport of vapor molecules inside the cylindrical pore, which is estimated to be close to 10 for a pore radius of 25 nm. Since the corresponding flow regime is Knudsen diffusion, the pressure drop in the gaseous phase is neglected. With this assumption, the balance of normal stress across the interface is given in terms of capillary and disjoining pressures by

$$p_{atm} - p_{li} = 2\sigma\kappa + \Pi_d \quad (9)$$

where the local mean curvature of the interface[29] and the disjoining pressure[30,31] are given by the following equations:

$$\kappa = \frac{1}{2}\left\{\frac{1}{r_i\left[1 + (\mathrm{d}r_i/\mathrm{d}x)^2\right]^{1/2}} + \frac{\mathrm{d}^2 r_i/\mathrm{d}x^2}{\left[1 + (\mathrm{d}r_i/\mathrm{d}x)^2\right]^{3/2}}\right\} \quad (10)$$

$$\Pi_d = \frac{-A}{6\pi(r_c - r_i)^3} + \frac{\varepsilon\varepsilon_o}{2(r_c - r_i)^2}\left(\frac{\pi k_B T_{li}}{Ze}\right)^2 \quad (11)$$

It is assumed that the value of surface tension remains close to bulk value even in the thin film region. Additionally, the retardation of dispersion force is neglected in this analysis, and the van der Waals component of disjoining pressure is evaluated using the nonretarded Hamaker's constant. The Hamaker's constant for two macroscopic phases 1 and 2 interacting across a medium 3 is calculated using the following equation[2]

$$A = \frac{3}{4}k_B T_{li}\left(\frac{\varepsilon_1 - \varepsilon_3}{\varepsilon_1 + \varepsilon_3}\right)\left(\frac{\varepsilon_2 - \varepsilon_3}{\varepsilon_2 + \varepsilon_3}\right) + \frac{3h\nu_e}{8\sqrt{2}}\frac{(n_1^2 - n_3^2)(n_2^2 - n_3^2)}{\sqrt{n_1^2 + n_3^2}\sqrt{n_2^2 + n_3^2}\left(\sqrt{n_1^2 + n_3^2} + \sqrt{n_2^2 + n_3^2}\right)} \quad (12)$$

where ε and n represent the dielectric constant and the refractive index of the interacting substances, respectively; k_B and h denote the Boltzmann's and Planck's constants, respectively; and ν_e denotes the absorption frequency, which is assumed to be 2.9 × 10^{15} s^{-1}.[32] According to eq 12, the Hamaker's constant varies slightly from -3.261×10^{-20} to -3.148×10^{-20} J corresponding to a temperature variation of 25 to 90 °C. In this analysis, a constant value of -3.148×10^{-20}J is assumed for the nonretarded Hamaker's constant.

The electrostatic interactions arise due to charging of the pore wall when it is submerged in an electrolyte, due to either a chemical reaction inducing charge dissociation or due to adsorption of charged species from the electrolyte. For instance, surface carboxylic groups could dissociate by losing protons to the electrolyte to become negatively charged. On the other hand, calcium ions from electrolyte could get adsorbed onto previously uncharged surfaces of lipid bilayers to result in a positively charged surface. In both cases, the total charge on the pore wall is balanced by an equal number of counter charges in the electrolyte. The disjoining pressure arising due to these electrostatic interactions is calculated using Langmuir's equation for thin films of dilute electrolyte on surfaces of high intrinsic electric potential. Langmuir's equation has been utilized to determine the electrostatic interactions between water and quartz surfaces. It is to be noted that Langmuir's equation offers simplicity and allows obtaining a critical insight to study the importance of electrostatic interaction. An alternative and more accurate analysis for a broader range of ionic strengths of electrolytes can be carried out by solving for charge and potential distribution in polar solvents. The electrostatic disjoining pressure can then be obtained from these distributions. Finally, the evaluation of disjoining pressure using eq 11 neglects the structural component due to lack of a well established and accepted relation to calculate structural forces as a function of film thickness.

The governing equation to determine the interfacial temperature gradient is derived from energy conservation applied to a differential volume as shown in Figure 1b. In this case, the net heat transferred to the control volume by conduction and advection causes evaporation of liquid at the interface. In order to simplify the energy conservation, the relative magnitudes of conduction and advection are assessed. The ratio of heat transferred by axial conduction ($\dot{q}_c \sim k_l A \Delta T / r_c$) and advection ($\dot{q}_a \sim \dot{m} C_{pl} \Delta T$) is estimated using the flow rate obtained from the dissipated heat flux from a single pore and the latent heat of evaporation, $\dot{m} \sim \dot{q}'' A / h_{fg}$. For a cylindrical pore of radius 25 nm and a reference heat flux of 1000 W/cm^2, the ratio of heat conduction to advection, $\dot{q}_c/\dot{q}_a \sim k_l h_{fg}/(\dot{q}'' C_{pl} r_c)$, is in excess of 1000. We choose the heat flux of ~1000 W/cm^2 in this work because this analysis has been motivated by application of evaporative cooling for thermal management of high performance electronic devices, which operate under high power dissipation loads. The analysis, however, is general enough and is applicable to other (lower and higher) heat fluxes supporting evaporation phase change within a nanopore. In this regard, the specific value of the heat flux is used only as a scaling parameter in the analysis. It will later be shown in the discussion of results that the heat flux used here for estimating the ratio is justified, and therefore, this approach is applicable even to pores of radius 500 nm. By neglecting advective heat transfer, the integral form of energy conservation is given by $\dot{q}_{c,r} - \dot{q}_{c,x} + \dot{q}_{c,x+\Delta x} = \dot{q}_e$. The net heat conducted along the axial direction, $\dot{q}_{c,x+\Delta x} - \dot{q}_{c,x} \simeq (\Delta x) \partial \dot{q}_{c,x} / \partial x$ is evaluated using the following equation, where Leibniz integral rule is again utilized.

$$\frac{\partial \dot{q}_{c,x}}{\partial x} = \frac{\partial}{\partial x} \int_{r_i}^{r_c} -k_l (2\pi r) \frac{\partial T_l}{\partial x} \, \mathrm{d}r$$

$$= (-2\pi k_l) \int_{r_i}^{r_c} r \frac{\partial^2 T_l}{\partial x^2} \, \mathrm{d}r + (2\pi k_l r_i) \left(\frac{\partial T_l}{\partial x} \right)_i \frac{\mathrm{d}r_i}{\mathrm{d}x} \quad (13)$$

A further simplification introduced in this analysis is a linear temperature variation in the radial direction. This approximation has been used previously for study of interfacial transport in microscopic pores and channels,[27] and should be equally applicable to nanoscale pores.

$$\frac{T_l - T_w}{T_{li} - T_w} = \frac{r - r_c}{r_i - r_c} \quad (14)$$

where T_{li} and T_w denote the temperature of the interface and the capillary wall, respectively. The governing equation for interfacial temperature distribution is obtained by using the linear temperature profile and the overall energy conservation. The derivation of this equation is included in the Supporting Information.

$$(2\pi k_l r_c) \frac{T_w - T_{li}}{r_c - r_i} + \frac{2\pi k_l}{3} (T_w - T_{li}) \left(\frac{\mathrm{d}r_i}{\mathrm{d}x} \right)^2$$
$$- \frac{2\pi k_l}{3} (r_c - r_i) \frac{\mathrm{d}r_i}{\mathrm{d}x} \frac{\mathrm{d}T_{li}}{\mathrm{d}x} + \frac{\pi k_l}{3} (r_c + 2r_i)(T_w - T_{li}) \frac{\mathrm{d}^2 r_i}{\mathrm{d}x^2}$$
$$- \frac{\pi k_l}{3} (r_c + 2r_i)(r_c - r_i) \frac{\mathrm{d}^2 T_{li}}{\mathrm{d}x^2} = - h_{fg} \frac{\mathrm{d}\dot{m}}{\mathrm{d}x} \quad (15)$$

Governing eqs 3, 8, 9, and 15 are used to determine the shape of the interface, flow rate, pressure, and temperature distribution. These equations are nondimensionalized using the following scaling parameters. The axial and radial coordinates are scaled with capillary radius, r_c as $\overline{x} = x/r_c$ and $\overline{r} = r_i/r_c$, while pressure, flow rate, and temperature are scaled as $\overline{p} = p_{li}/p_v$, $\overline{\dot{m}} = \dot{m}/\dot{m}_o$ and $\overline{T}_i = 2\pi r_c k_l (T_{li} - T_w)/\dot{m}_o h_{fg}$, respectively. The mass flow rate, $\dot{m}_o$, used for scaling other dependent variables is given by the following equation, where $p_{v,eq}(T_w)$ denotes the saturation pressure at temperature T_w.

$$\dot{m}_o = \frac{2\hat{\sigma}}{2 - \hat{\sigma}} \left(\frac{M}{2\pi R T_w} \right)^{1/2} \left[p_{v,eq}(T_w) - p_v \right] (2\pi r_c{}^2) \quad (16)$$

The nondimensional form of governing equations is summarized below, where Π_i denote the nondimensional parameters resulting from scaling flow variables. It is to be noted that, in deriving the nondimensional form of mass flux from evaporation kinetics (eq 8), the Clausius–Clapeyron relation ($\mathrm{d}P/\mathrm{d}T = \rho_v h_{fg}/T$) has been used to determine the equilibrium vapor pressure as a function of temperature. A brief derivation of this equation is provided in the Supporting Information.

$$\overline{\dot{m}} = \frac{\pi}{8} \Pi_1 \left(-\frac{\mathrm{d}\overline{p}_{li}}{\mathrm{d}\overline{x}} \right) \left[(1 - \overline{r}_i{}^2)(1 - 3\overline{r}_i{}^2) - 4\overline{r}_i{}^4 \ln \overline{r}_i \right]$$
$$+ \frac{1}{16} \Pi_2 \left(\frac{\mathrm{d}\overline{T}_i}{\mathrm{d}\overline{x}} \right) \left[4\overline{r}_i (1 - \overline{r}_i{}^2) + 8\overline{r}_i{}^3 \ln \overline{r}_i \right] \quad (17)$$

$$\left(1 + \frac{1}{2\pi} \Pi_3 \Pi_4 \overline{T} \right) \left(1 + \frac{1}{2\pi} \Pi_4 \overline{T} \right)^{-1/2}$$
$$= \frac{-1}{\overline{r}_i \left[1 + (\mathrm{d}\overline{r}_i/\mathrm{d}\overline{x})^2 \right]^{1/2}} \frac{\mathrm{d}\overline{\dot{m}}}{\mathrm{d}\overline{x}} \quad (18)$$

$$\Pi_5 - \overline{p}_{li} = \Pi_6 \left\{ \frac{1}{\overline{r}_i \left[1 + (\mathrm{d}\overline{r}_i/\mathrm{d}\overline{x})^2 \right]^{1/2}} + \frac{\mathrm{d}^2 \overline{r}_i / \mathrm{d}\overline{x}^2}{\left[1 + (\mathrm{d}\overline{r}_i/\mathrm{d}\overline{x})^2 \right]^{3/2}} \right\}$$
$$+ \frac{\Pi_7}{6\pi (1 - \overline{r}_i)^3} + \Pi_8 \left(\frac{1 + \Pi_4 \overline{T}/2\pi}{1 - \overline{r}_i} \right)^2 \quad (19)$$

$$\frac{-\overline{T}_i}{1 - \overline{r}_i} - \frac{\overline{T}_i}{3} \left(\frac{\mathrm{d}\overline{r}_i}{\mathrm{d}\overline{x}} \right)^2 - \frac{(1 - \overline{r}_i)}{3} \frac{\mathrm{d}\overline{r}_i}{\mathrm{d}\overline{x}} \frac{\mathrm{d}\overline{T}_i}{\mathrm{d}\overline{x}} - \frac{\overline{T}_i}{6} (1 + 2\overline{r}_i) \frac{\mathrm{d}^2 \overline{r}_i}{\mathrm{d}\overline{x}^2}$$
$$- \frac{(1 + 2\overline{r}_i)(1 - \overline{r}_i)}{6} \frac{\mathrm{d}^2 \overline{T}_i}{\mathrm{d}\overline{x}^2} = - \frac{\mathrm{d}\overline{\dot{m}}}{\mathrm{d}\overline{x}} \quad (20)$$

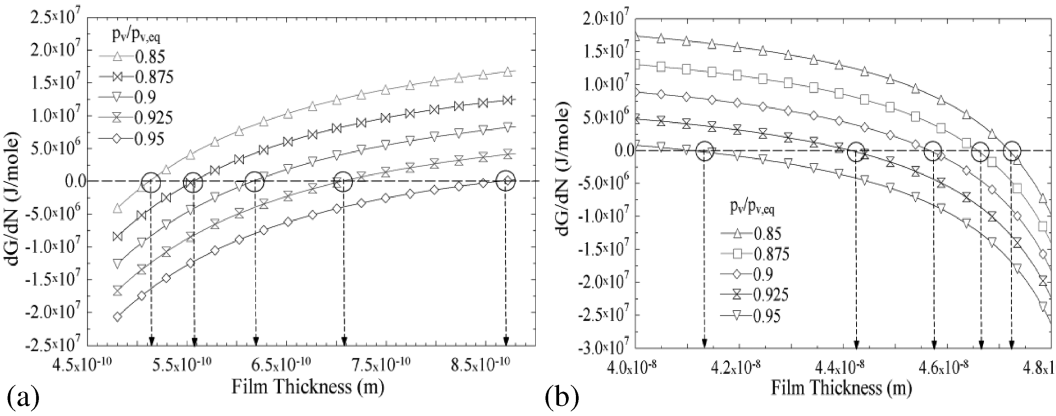

Figure 2. The adsorbed film thickness corresponding to $\partial G/\partial N = 0$ and (a) $\partial^2 G/\partial N^2 > 0$, (b) $\partial^2 G/\partial N^2 < 0$, calculated at different vapor pressures for $r_c = 30$ nm and $T_w = 90$ °C.

The nondimensional parameters are defined as

$$\Pi_1 = \frac{\rho_l {r_c}^3 p_v}{\mu_l \dot{m}_o} \quad \Pi_2 = \frac{\rho_l r_c h_{fg}}{\mu_l k_l}\left(\frac{d\sigma}{dT}\right)$$

$$\Pi_3 = \frac{\rho_v(T_w)h_{fg}}{p_{v,eq}(T_w) - p_v} \quad \Pi_4 = \frac{\dot{m}_o h_{fg}}{r_c k_l T_w} \quad \Pi_5 = \frac{p_{atm}}{p_v}$$

$$\Pi_6 = \frac{\sigma}{r_c p_v} \quad \Pi_7 = \frac{-A}{{r_c}^3 p_v} \quad \Pi_8 = \frac{\varepsilon\varepsilon_o}{2p_v}\left(\frac{\pi k T_w}{Zer_c}\right)^2$$

The ratio of nondimensional parameters, Π_2/Π_1, compares the pressure gradient arising from thermocapillary effect to the total pressure gradient driving the flow in the meniscus. Π_4 represents a ratio of radial temperature drop across the extended meniscus to the wall temperature. The characteristic value of Π_4 is typically small ($\sim 10^{-3}$ to 10^{-2}) for evaporation inside nanopores or channels. Π_6, Π_7, and Π_8 compare pressures arising due to capillary, van der Waals, and electrostatic interactions.

Equations 17−20 are numerically integrated using the Runge−Kutta method to obtain the location of the interface, pressure, and mass flow rate as a function of the axial variable. Due to the singularity $d\bar{r}_i/d\bar{x} \rightarrow \infty$ as $\bar{r}_i \rightarrow 0$, numerical convergence could not be achieved in the vicinity of $\bar{r}_i = 0$. In order to obtain the solution at $\bar{r}_i = 0$, the governing equations were transformed from $\bar{x}$ to $\bar{r}_i$ dependence to facilitate integration with respect to $\bar{r}_i$. By adopting this procedure, convergence was easily achieved since $d\bar{x}/d\bar{r}_i \rightarrow 0$ as $\bar{r}_i \rightarrow 0$. The transformed governing equations can also be found in the Supporting Information.

The boundary conditions at $\bar{x} = 0$ required to integrate eqs 17−20 are $\bar{r}_i = \bar{r}_o$, $d\bar{r}_i/d\bar{x} = 0$, $\bar{m} = 0$, $\bar{p} = \Pi_5 - \Pi_6/\bar{r}_o - \Pi_7/(1 - \bar{r}_o)^3 - \Pi_8/(1 - \bar{r}_o)^2$, $\bar{T} = 0$, and $d\bar{T}/d\bar{x} = 0$ where $\bar{r}_o$ denotes the equilibrium radius, which is related to thickness of the adsorbed film as $\bar{r}_o = 1 - \bar{t}_o$. The following section describes the procedure used to calculate the adsorbed film thickness.

3. EQUILIBRIUM THICKNESS OF AN ADSORBED FILM

The thickness of the adsorbed film on a pore or channel wall is determined by various factors that define equilibrium between the condensed and gas phases. Kelvin's relation was based on equilibrium between a capillary held liquid and its vapor phase. In the case of capillary rise, the equation takes the form $p_{v,eq} - p_{vi} = \sigma\kappa\rho_v/(\rho_l - \rho_v)$ where $p_{v,eq}$ and p_{vi} represent the vapor pressure in equilibrium with the liquid for a plane and curved interface, respectively.[22] A modification to Kelvin's equation proposed by Cohen incorporates gas adsorption on the walls of cylindrical pores. The resulting isothermal jump in equilibrium vapor pressure of a pure liquid−vapor system at temperature T due to the presence of an adsorbed film of thickness t in a pore of radius r_c is given by the following equation.[33]

$$(\rho_l RT/M)\ \ln(p_{vi}/p_{v,eq}) = -\sigma/(r_c - t) \tag{21}$$

Using eq 21, the change in the equilibrium vapor pressure due to a curved meniscus, with an effective capillary radius ($r_c - t$) of 25 nm, at a temperature $T \sim 90$ °C is estimated to be less than 2%. Therefore, in this analysis the equilibrium vapor pressure p_{vi} is calculated from saturation properties of water as a function of temperature.

A thermodynamic treatment of phase change in the cylindrical pore was later presented by de Boer,[34] elucidating the hysteresis observed during capillary condensation and evaporation of simple dielectric fluids. The derivation of equilibrium film thickness presented herein is an extension of de Boer's study by incorporating the formulation of disjoining pressure by Derjaguin[30] and including electrostatic interactions in polar liquids as given by Langmuir.[30,31]

The thickness of an adsorbed layer in a liquid−vapor system confined inside a pore or channel is governed by the equilibrium established between the condensing (gas) and evaporating (liquid) phases. At a fixed pressure and temperature, the change in free energy of this thermodynamic system when dN moles of gas condense is given by $dG_{p,T} = \Sigma((\partial G)/(\partial N))_{p,T}dN$. The factors affecting the free energy of the system during capillary condensation or evaporation are the chemical potential of interacting phases, the surface tension and the disjoining pressure. These are mathematically expressed as $\hat{\mu} = (\partial G/\partial N)_{p,T}$, $\sigma = (\partial G/\partial S)_{p,T}$, and $\Pi_d = (-1/S)(\partial G/\partial t)_{p,T}$, where S represents the surface area of the interface, t corresponds to the film thickness, and Π_d represents the disjoining pressure experienced by the condensed phase in contact with the pore. These factors affecting the net change in free energy are incorporated in the analysis as shown below:

$$dG_{p,T} = \left(\frac{\partial G}{\partial N}\right)_{p,T} + \left(\frac{\partial G}{\partial S}\right)_{p,T}\frac{dS}{dN} + \left(\frac{\partial G}{\partial t}\right)_{p,T}\frac{dt}{dN} \tag{22}$$

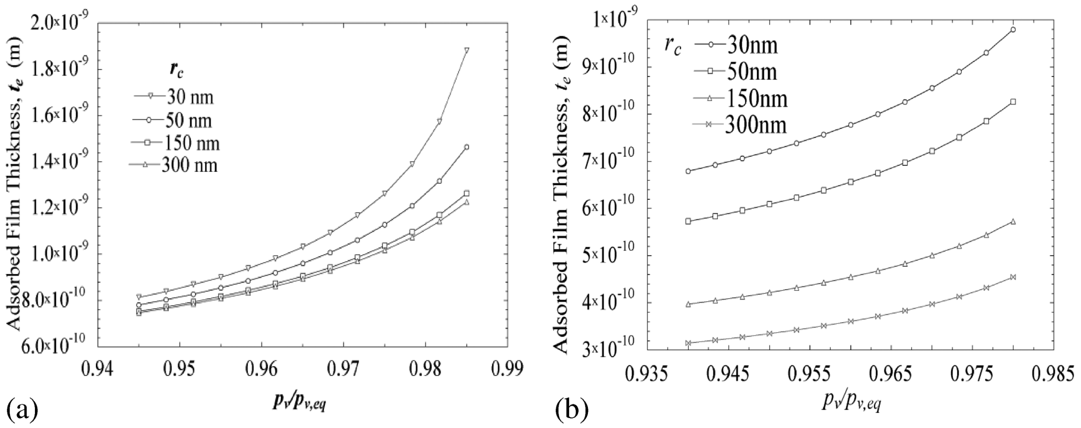

Figure 3. (a) The adsorbed film thickness calculated at $T_w = 90$ °C for different capillary radii and vapor pressures used in the model described in this work. (b) Adsorbed film thickness calculated using eq 26, which neglects electrostatic interactions.

Using equations relating variables N, S, and t, which are $dS/dN = -V_m/(r - t)$ and $dt/dN = V_m/A$ where V_m represents the molar volume of the condensed phase, the transformed eq 23 illustrates how both capillary and disjoining pressure can affect the free energy of the system during a phase-change process.

$$\frac{\partial G}{\partial N_{p,T}} = \hat{\mu}_c - \hat{\mu}_g - \frac{\sigma}{(r_c - t)} V_m - \Pi_d V_m \tag{23}$$

where the difference in the chemical potential $(\hat{\mu}_c - \hat{\mu}_g)$ in eq 23 can be represented in terms of pressure and temperature, $RT \ln(p_{v,eq}/p_v)$ for an ideal solution, where $p_{v,eq}$ is the saturation pressure at temperature T and p_v is the partial pressure of vapor in the air−vapor mixture surrounding the interface.

In order to establish equilibrium, the free energy should attain a minimum, which requires two conditions to be satisfied, namely, $(\partial G/\partial N)_{p,T} = 0$ and $(\partial^2 G/\partial N^2)_{p,T} > 0$. Hence, the equilibrium film thickness is determined from the following two relations:

$$(\rho_l RT/M) \ln(p_{v,eq}/p_v) - \frac{\sigma}{(r_c - t_e)} - \Pi_d = 0 \tag{24}$$

$$-\frac{\sigma}{(r_c - t_e)^2} - \frac{d\Pi_d}{dt} \geq 0 \tag{25}$$

In deriving relation 25, the relation $dt/dN > 0$ has been used, which implies a growth in the film as vapor molecules are transferred from gas phase to the condensed layer. The values of film thickness for water at 90 °C confined inside a capillary of radius 30 nm and satisfying eq 24 for different values of relative pressure $p_v/p_{v,eq}$ are shown in Figure 2a,b. Evidently, there are multiple solutions of eq 24 as illustrated by circled data points in Figure 2a,b, but only those values satisfying inequality 25 can establish a stable equilibrium. These values are marked in Figure 2a, which correspond to the conditions $\partial G/\partial N = 0$, as well as $\partial^2 G/\partial N^2 > 0$.

The equilibrium thickness of the adsorbed film is a function of three parameters, namely, the temperature, the vapor-pressure ratio, and the capillary radius. The adsorbed thickness as a function of capillary radius and vapor-pressure ratio is shown for water at a temperature of 90 °C in Figure 3a. The partial pressure of vapor, p_v, in the gas phase surrounding the interface is governed by the rate of vapor transport away from interface. In other words, the ambient is relatively dry when vapor removal from the near interface zone via diffusion and/or advection is efficient, and it is humid when gas phase mass transfer is poor and the process is mass transport limited. An increase in the vapor pressure of the ambient causes a decrease in the net driving potential for evaporation, resulting in a thicker adsorbed film in equilibrium with vapor. On the other hand, a decrease in the capillary radius also results in thicker adsorbed film for a given vapor pressure ratio. As the effective capillary radius decreases, the molecules at the free surface are more closely held by the neighboring surface molecules resulting in thicker equilibrium films. A constant decrease in capillary radii can potentially drive the system closer to equilibrium if the ambient is sufficiently saturated. This phenomenon is indeed observed during capillary condensation and evaporation and explains the hysteresis observed in the isotherms during adsorption and desorption.[34] It is to be noted that a fixed value of surface tension for water is assumed in this analysis to determine the equilibrium film thickness. Due to the interaction between ultrathin liquid film and the substrate, the thickness dependence of the surface tension is obtained by the integration of the corrected van der Waals pressure equation.[35] The deviation in the value of surface tension for very thin liquid films (~1 nm) from its bulk value, at a fixed temperature, was found to be within 3%. Therefore, while the temperature dependence of surface tension is included to account for the thermocapillary effect, the thickness effect is neglected due to its relatively minor contribution. The formulation presented in this study to calculate the equilibrium film thickness differs from that initially proposed by Wayner et al.[12]

$$t_e = \left[\frac{-AV_m T_v}{6\pi M h_{fg}(T_{li} - T_v)}\right]^{1/3} \tag{26}$$

which was later adopted in many subsequent studies. The derivation of eq 26, applicable only to nonpolar solvents, is based entirely on evaporation kinetics and bears no information on the free energy of the liquid−vapor system. It is also evident that this formulation cannot be utilized in systems where the condensed phase is in thermal equilibrium with its gas phase, while it is indeed possible for an unsaturated vapor phase to be in thermal equilibrium with its liquid phase, by establishing a nonevaporating adsorbed layer. The interfacial temperature jump, $(T_{li} - T_v)$, and vapor temperature, T_v, required for computing the adsorbed film thickness in eq 26 are commonly postulated as a priori

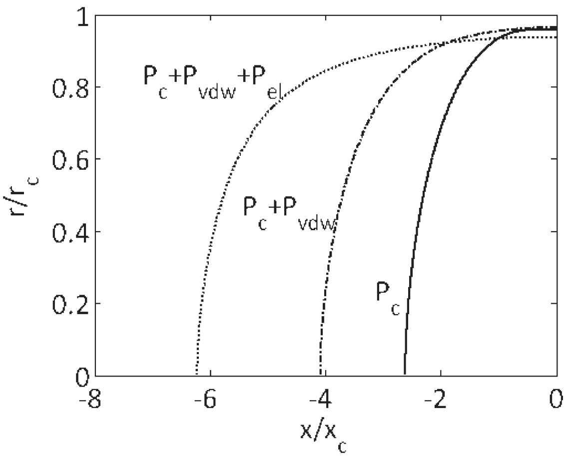

Figure 4. Effect of capillary and disjoining pressure on the shape of the interface is illustrated. The extension of meniscus due to electrostatic interaction is also shown. The interface is shown for the simulation conditions of r_c = 30 nm, T_w = 90 °C, and $p_v/p_{v,eq}$ = 0.98.

known parameters; however, for a self-consistent comparison of our approach (based on local thermal equilibrium between phases) to that of Wayner et al.,[12] the temperature jump and vapor temperature are scaled by $\dot{m}_o h_{fg}/(2\pi_{rc}k_l)$ and T_w, respectively, to calculate equilibrium film thickness, with evaporation rate $\dot{m}_o$ given by eq 16. Figure 3b shows variation of adsorbed film thickness calculated using eq 26 for different capillary radii and vapor pressures, using $(T_{li} - T_v)$ and T_v, estimated as outlined above. Comparing results in Figure 3a and b shows that an increase in the adsorbed film thickness with capillary radius and relative vapor pressure is observed in both cases, with difference in magnitude within a factor of 2. This mismatch is due to inclusion of electrostatic interactions as well as the procedure used for estimating the temperature jump in terms of the evaporation rate.

4. RESULTS AND DISCUSSION

The governing equations are solved to obtain the shape of the interface, mass flow rate, pressure, and temperature distribution inside the capillary. The importance of including electrostatic disjoining pressure is discussed. The effects of thermocapillary stresses are also presented for different operating conditions. The three operational parameters identified to be critical in the resulting flow characteristics are the radius of the capillary, r_c, the wall temperature, T_w, and the relative vapor-pressure, $p_v/p_{v,eq}$. The interface shown in all simulations is assumed to be pinned at $\bar{x} = 0$, which also marks the boundary of adsorbed film in equilibrium with the ambient vapor phase. The temperature dependent properties of water used for all calculations are listed in the Supporting Information. In order to build intuitive understanding of the problem in hand, we describe the results in terms of physical (dimensional) parameters. A brief discussion of the results in terms of the relevant nondimensional groups is also included where necessary to support the generality of our conclusions.

4.1. Capillary and Disjoining Pressures. The relative effects of capillary and disjoining pressures on the shape of the interface are compared in Figure 4, corresponding to r_c = 30 nm, T_w = 90 °C, and $p_v/p_{v,eq}$ = 0.98. During evaporation, the interface acquires a distinct shape to balance the viscous stresses and pressure forces. The total interface area of the meniscus inside a capillary tube is smallest when only capillary pressure is considered, while it is largest when capillary and disjoining pressures are both included in the analysis. Away from the pore-wall, where capillary forces are significantly larger than disjoining pressure, the meniscus is highly curved, resulting in higher gradient in capillary pressure to balance the viscous pressure drop inside the liquid. On the other hand, the interface is less curved and the change in slope is more gradual when disjoining pressure is significant in addition to capillary pressure near the pore wall. The presence of electrostatic interaction in addition to van der Waals forces enhances the disjoining pressure, causing a further reduction in the gradient in the curvature required to balance the viscous stress.

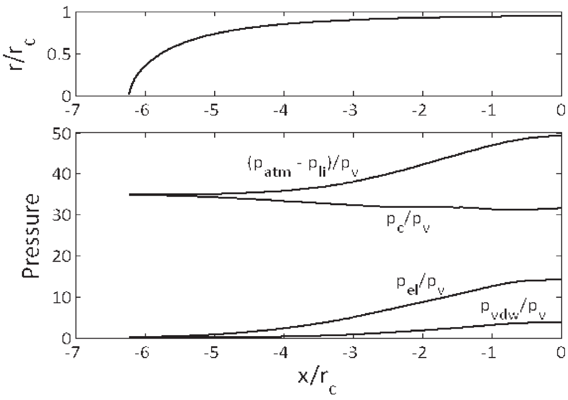

Figure 5. Axial variation of normalized capillary and disjoining pressures (electrostatic and van der Waals components) along a meniscus interface inside a cylindrical pore (r_c = 30 nm, T_w = 90 °C, and $p_v/p_{v,eq}$ = 0.98).

The relative magnitudes of various forces acting on the interface are shown in Figure 5 in terms of relative pressure along the axial position. The nondimensional variables corresponding to r_c = 30 nm, T_w = 90 °C, and $p_v/p_{v,eq}$ = 0.98 are of the following orders of magnitude: $\Pi_6 = 3 \times 10^1$, $\Pi_7 = 9 \times 10^{-4}$, and $\Pi_8 = 6 \times 10^{-2}$, which indicate the relative strengths of capillary, van der Waals, and electrostatic interactions, respectively. It is clear that capillary pressure is a dominant force in nanopores compared to disjoining pressure. The magnitudes of van der Waals and electrostatic interactions are comparable to capillary pressure only at close proximities of $\bar{r}_i > 0.96$ and $\bar{r}_i > 0.95$ to the wall, respectively. Interestingly, the equilibrium radius of the adsorbed film for these conditions is $\bar{r}_o = 0.9373$. This suggests that the capillary pressure is significant in a large portion of the extended meniscus; also, since even the adsorbed film inside a cylindrical pore has a nonzero curvature, the capillary forces are significant along the entire length of the meniscus in small pores (~30 nm).

While the absolute pressure of the liquid phase is mainly determined by the capillary pressure, the disjoining pressure demonstrates a much larger gradient in the thin film region ($\bar{x} \rightarrow 0$). Since it is the total pressure gradient that drives fluid flow, the contribution of electrostatic interaction is significant as shown in Figure 5, and is even greater than that due to capillary forces. Also, the capillary forces and disjoining (electrostatic together with van der Waals) pressure forces act in opposite directions, as reflected in different sign of pressure gradients.

While it is the pressure gradient (not an absolute value of pressure), which determines fluid flow in the extended meniscus inside the capillary, it is useful and relevant to the current analysis to describe the state of liquids confined in very small capillaries.

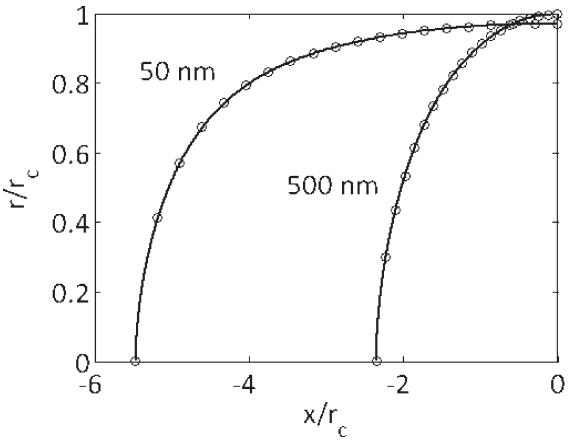

Figure 6. Effect of thermocapillary (Marangoni) stresses for water confined in nanocapillaries. The shape of interface in capillaries of different radii, as predicted with (solid lines) and without (circles) Marangoni stresses included in the analysis. The interfaces are shown for $T_w = 90$ °C and $p_v/p_{v,eq} = 0.98$.

It is known that liquids in tension can sustain extremely large negative pressures. In particular, it has been reported that water in hydrophilic nanochannels can exist under large negative pressures while being metastable.[36,37] The derivation of an equilibrium film thickness shown previously in this study is in accordance with the general stability criteria for metastable liquids. We adopt a phenomenological approach[38] to determine the equilibrium conditions for metastable liquids and fluid mixtures. Additionally, the laws of hydrodynamics governing liquid flow are still applicable in this case, since the approximation of a continuum phase is not violated.

4.2. Thermocapillary Stresses in Cylindrical Pores. In order to determine the effect of Marangoni stress on interfacial transport, the shape of the interface is calculated for two distinct operating conditions. At $T_w = 90$ °C and $p_v/p_{v,eq} = 0.98$, the interfaces corresponding to capillary radii of 50 and 500 nm are shown in Figure 6. For both radii, since $\Pi_1/\Pi_2 > 40$, the ratio of viscous to thermocapillary stress is large, which indicates that Marangoni stresses are comparatively less significant in nanocapillaries. The shape outlined by open circles is for viscous-shear-only transport, and is qualitatively compared with the solid curves when Marangoni stresses are included. It is clear that the inclusion of thermocapillary stresses in the analysis results in a negligible change in the interface shape for both 50 and 500 nm pores. This is expected, since Marangoni stresses are prominent only in much larger capillaries with large temperature gradient along the interface. In this analysis, with water as the evaporating liquid, the temperature gradient is not substantial to affect the flow behavior even in 500 nm capillaries.

4.3. Effect of Capillary Radius. The interface corresponding to different capillary radii at a constant wall temperature and vapor pressure of $T_w = 90$ °C and $p_v/p_{v,eq} = 0.98$, respectively, is shown in Figure 7 in terms of nondimensional radial and axial coordinates. As evident from eq 19, the nondimensional parameters that control the interfacial shape and transport during evaporation are Π_6, Π_7, and Π_8, which compare the relative importance of capillary, van der Waals, and electrostatic interactions, respectively. Relative magnitude of these nondimensional numbers for different capillary radii is indicative of the resulting interfacial shape.

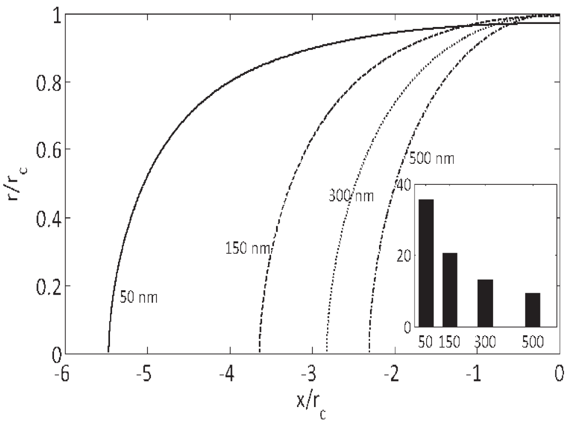

Figure 7. Interface shape corresponding to $T_w = 90$ °C, $p_v/p_{v,eq} = 0.98$, and $r_c = 50$ to 500 nm. The inset compares the average evaporating mass flux (kg/m^{2}s) at different capillary radii (nm).

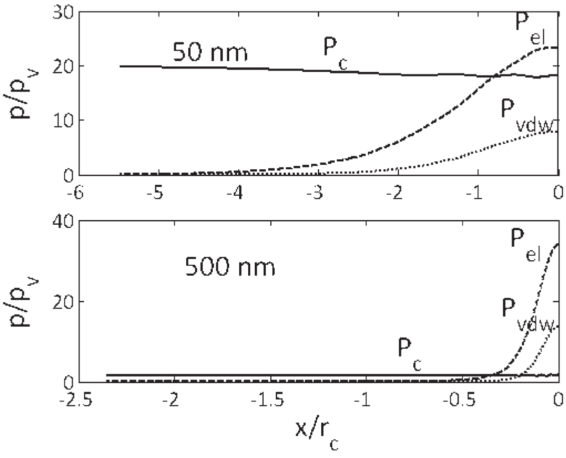

Figure 8. Comparison of capillary and disjoining pressures along the meniscus in capillaries at $T_w = 90$ °C, $p_v/p_{v,eq} = 0.98$, and pore radii of $r_c = 50$ nm and 500 nm, respectively.

In the case of a capillary pore of radius 500 nm, the nondimensional numbers $\Pi_6 \approx 2$, $\Pi_7 \approx 2 \times 10^{-7}$, and $\Pi_8 \approx 2 \times 10^{-4}$ differ substantially from those for a capillary pore of radius 50 nm, for which $\Pi_6 \approx 2 \times 10$, $\Pi_7 \approx 2 \times 10^{-4}$, and $\Pi_8 \approx 2 \times 10^{-2}$. While these values clearly indicate that capillary effect plays a key role in both cases, it is also evident that the relative importance of van der Waals and electrostatic interactions are greater in smaller pores, which results in a further extension of the meniscus, as demonstrated in Figure 7.

The shape of interface during evaporation also depends on the pressure gradient driving the flow. For instance, the axial variation of capillary and disjoining pressures is shown in Figure 8 for cylindrical pores of radii 50 and 500 nm. The total pressure gradient is due to both capillary and disjoining pressures, as shown in Figure 8. In the case of narrow pores, while capillary pressure is greater in magnitude, the disjoining pressure is significant over a larger portion of the interface. This observation is supported by the relative magnitudes of nondimensional parameters Π_6,Π_7, and Π_8. Also, Figure 8 demonstrates a substantial gradient in both capillary and disjoining pressures over a much larger portion of the interface for smaller pores. Consequently, fluid flow can be

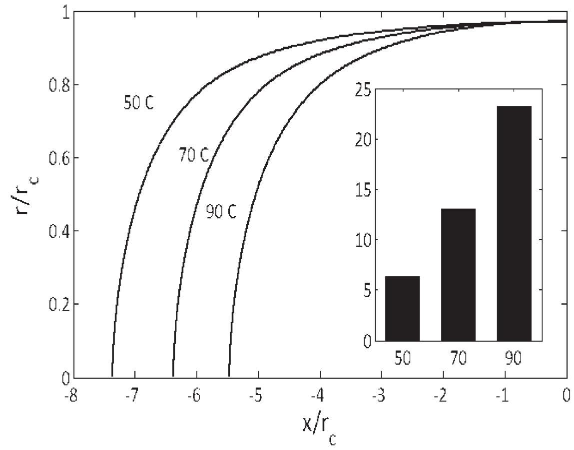

Figure 9. Interface corresponding to $p_v/p_{v,eq}$ = 0.98, r_c = 50 nm, and varying pore wall temperatures, T_w = 50, 70, and 90 °C. The inset compares the average mass flux (kg/m^{2}s) at different wall temperatures (°C).

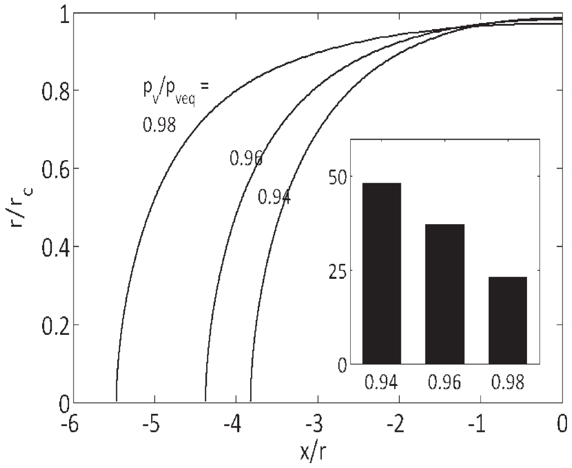

Figure 10. Interface corresponding to r_c = 50 nm, T_w = 90 °C, and varying the relative pressure in the ambient environment surrounding the meniscus $p_v/p_{v,eq}$ = 0.98, 0.96, and 0.94. The inset compares the average mass flux (kg/m^{2}s) at different vapor pressures.

sustained over relatively long and significantly thinner film regions in smaller capillaries. It is the absence of a significant pressure gradient in large capillaries that results in a much smaller meniscus length relative to the capillary radius. Consequently, it can be established from Figure 7, which shows interfacial shape in nondimensional units, that the total length of the interface does not increase proportionally with the capillary radius.

The ability of smaller pores to sustain fluid flow through relatively longer, thin film regions results in a larger rate of evaporation per unit pore cross-sectional area. This is shown in Figure 7 as an inset comparing average evaporation mass flux for different pore radii. It is noteworthy to mention that, if the ambient gas phase can be maintained sufficiently dry to remove external mass transfer limitations, then large heat fluxes can be sustained through evaporation. For the mass fluxes given in the inset of Figure 7, the net evaporation corresponds to heat fluxes ($\dot{m}''h_{fg}$) in excess of 1000 W/cm^2.

4.4. Effect of Wall Temperature and Vapor Pressure. Figure 9 compares the shape of the interface corresponding to different wall temperatures. The total length of the interface is smaller at higher temperatures, but yields larger average evaporation rate in a pore, as shown in the inset in Figure 9. Since the temperature jump across the interface between the liquid and gas phases is neglected in this analysis, a higher evaporation rate for a fixed pore radius is mainly a result of higher equilibrium vapor pressure at higher temperatures. As a result, a larger gradient in the curvature of interface is expected in order to support a higher flow rate in the thin film region. The total length of the interface is therefore much smaller for evaporation at higher temperatures. Figure 10 compares the shape of interface resulting from varying the vapor pressure of the ambient atmosphere surrounding the evaporating meniscus for a fixed wall temperature and capillary radius. The average mass flux per unit pore footprint area (πr_c^2) is directly proportional to the difference of pressure at the interface, ($p_{vi} - p_v$), as shown in eq 8. Therefore, analogous to the effect temperature, the length of the interface shrinks for smaller vapor pressure ratios, $p_v/p_{v,eq}$, due to higher flow rate in the thin film region.

5. SUMMARY AND CONCLUSION

Analysis of interfacial transport is carried out for water evaporating in the confines of a cylindrical nanopore. The governing equations for fluid flow and heat transfer are derived in the limit of continuum transport. In addition to capillarity and dispersion forces, the analysis incorporates the electrostatic interaction in a solid–liquid–vapor system using the Langmuir equation and demonstrates its effect on the interfacial characteristics. A thermodynamic approach to the calculation of equilibrium film thickness is presented, which differs from the conventional formulation[12] that relies only on evaporation kinetics. The governing, nonlinear differential equations are solved numerically to determine the axial variation of flow variables and the shape of the interface under various operating conditions.

At a constant wall temperature, the equilibrium thickness of adsorbed film is found to increase with the relative vapor pressure, $p_v/p_{v,eq}$, while it decreases with increase in pore radius, r_c. An increase in the vapor pressure of the ambient environment causes a reduction in the external driving potential for evaporation, resulting in a thicker adsorbed film in equilibrium with its vapor phase. On the other hand, as the capillary radius decreases, the molecules at the free surface are more strongly held by the neighboring surface molecules resulting in thicker equilibrium films.

This study also demonstrates a significant change in the shape of the interface when electrostatic interactions are included, in addition to van der Waals and capillary forces. In particular, the interface is found to extend further due to electrostatic forces. Therefore, the net rate of evaporation is promoted due to an increase in the total free surface area, as well as owing to an enlarged thin film region in the meniscus.

The inclusion of thermocapillary stress does not yield measurable variation in interfacial characteristics for nanoscale capillaries, due to insufficient temperature gradient to induce stresses comparable to other driving forces.

The analysis identifies three important parameters that significantly affect the overall performance of the system, namely, the capillary radius, wall temperature, and the degree of saturation of vapor phase. In smaller capillaries, the viscous pressure drop is supported by a significant gradient in both disjoining and capillary pressures over a large fraction of the meniscus. In larger capillaries, the pressure gradient is significant only at the leading edge of the entire meniscus, where the contribution of the disjoining pressure is important. As a result, the extension of meniscus is prominent for smaller nanoscale capillaries, in turn, yielding a greater net rate of evaporation per unit pore area.

The effects of temperature and ambient vapor pressure on net rate of evaporation are shown to be analogous. An increase in wall temperature, which enhances saturation pressure, or a decrease in the ambient vapor pressure, both result in an overall increase in the net potential for evaporation from the interface. Also, since a higher rate of evaporation requires a larger pressure gradient inside the meniscus, the length of the meniscus shrinks for higher evaporation fluxes to accommodate higher gradients.

The results of this analysis are important not only from a fundamental prospective, but also for advancing numerous applications, from water distillation[39−42] to thermal management of high power sources,[43,44] which take advantage of highly efficient phase change in nanoporous systems.

■ ASSOCIATED CONTENT

Ⓢ **Supporting Information.** Derivation and brief description of governing equations which are numerically integrated to determine flow variables. Table of thermophysical properties of water used in this analysis. This material is available free of charge via the Internet at http://pubs.acs.org.

■ AUTHOR INFORMATION

Corresponding Author

*E-mail: AGF@gatech.edu. Phone: 404-385-1356. Fax: 404-894-8496.

■ ACKNOWLEDGMENT

The authors acknowledge the support of the Interconnect Focus Center, one of five research centers funded under the Focus Center Research Program, a DARPA and Semiconductor Research Corporation program.

■ NOMENCLATURE

A - Hamaker's Constant (J)
d - Diameter of water molecule (m)
e - Elementary charge (C)
G - Gibbs free energy (J)
h - Planck's constant ($6.626\,068 \times 10^{-34}$ m^2 kg/s)
h_{fg} - Enthalpy of vaporization (J/kgK)
k_B - Boltzmann constant ($1.380\,650\,3 \times 10^{-23}$ m^2 kg s^{-2} K^{-1})
k_l - Thermal conductivity of the liquid (W/mK)
K_n - Knudsen number for vapor diffusion in a nanocapillary
M - Molecular weight (kg/kmol)
N - Number of moles of evaporating/condensing molecules (mole)
N_A - Avogadro's constant
$\dot{m}_o''$,$\dot{m}_o$ - Mass flux and mass flow rate at reference conditions, respectively (kg/m^2 s, kg/s)
n - Refractive index of a medium
p_{atm} - Atmospheric pressure (Pa)
p_l, p_v - Pressure of liquid and partial pressure of vapor phase, respectively (Pa)
p_{vi}, $p_{v,eq}$ - Equilibrium vapor pressure of curved and flat interface, respectively (Pa)
$\dot{q}_a$, $\dot{q}_c$ - Rate of heat advection and conduction, respectively (W)
R - Universal gas constant (J/kmolK)
r - Radial coordinate (m)
r_c - Radius of the capillary or pore (m)
r_i - Radial position of the interface (m)
t_e - Equilibrium thickness of the adsorbed film (m)
T_l, T_v - Temperature of the liquid and gas phase, respectively (K)
u_l, v_l - Axial and radial components of the liquid velocity inside the meniscus, respectively (m/s)
V_m - Molar volume of the evaporating liquid (m^3/kmol)
w_{li} - Velocity of the liquid phase normal to the interface (m/s)
x - Axial coordinate (m)
Z - Charge of a dissociated ion

■ GREEK SYMBOLS

ε - Dielectric constant
ε_o - Permittivity of free space
κ - Curvature of the meniscus (m^{-1})
μ_l - Absolute viscosity of the liquid (kg/ms)
$\hat{\mu}$ - Chemical potential (J/kmol)
ν_e - Absorption frequency (s^{-1})
Π_d - Disjoining pressure (Pa)
ρ_l, ρ_v - Density of liquid and vapor phase, respectively (kg/m^3)
σ - Surface tension of liquid (N/m)
$\hat{\sigma}$ - Accommodation coefficient
θ - Slope of the interface at any axial location

■ REFERENCES

(1) de Gennes, P. G. *Rev. Mod. Phys.* **1985**, *57*, 827.
(2) Israelachvili, J. N. *Intermolecular and Surface Forces*, 3rd ed.; Academic Press: London, 1992.
(3) Rabinovich, Y. I.; Derjaguin, B. V.; Churaev, N. V. *Adv. Colloid Interface Sci.* **1982**, *16*, 63–78.
(4) Derjaguin, B. V. *Acta Physicochim. USSR* **1941**, *14*, 633–662.
(5) Verwey, E. J. W. *J. Phys. Chem.* **1947**, *51*, 631–636.
(6) Pashley, R. M.; Kitchener, J. A. *J. Colloid Interface Sci.* **1979**, *71*, 491–500.
(7) Deryagin, B. V.; Churaev, N. V. *Langmuir* **1987**, *3*, 607–612.
(8) Deryagin, B. V.; Popovskii, Y. M.; Goryuk, A. A. *Langmuir* **1987**, *3*, 628–631.
(9) Gee, M. L.; Healy, T. W.; White, L. R. *J. Colloid Interface Sci.* **1990**, *140*, 450–465.
(10) Pashley, R. M. *Adv. Colloid Interface Sci.* **1982**, *16*, 57–62.
(11) Ninham, B. W. *Adv. Colloid Interface Sci.* **1999**, *83*, 1–17.
(12) Wayner, P. C.; Kao, Y. K.; LaCroix, L. V. *Int. J. Heat Mass Transfer* **1976**, *19*, 487–492.
(13) Wayner, P. C., Jr. *AIAA J.* **1979**, *17*, 772–776.
(14) DasGupta, S.; Schonberg, J. A.; Wayner, P. C., Jr. *ASME Trans. J. Heat Transfer* **1993**, *115*, 201–208.
(15) Buffone, C.; Sefiane, K. *Int. J. Multiphase Flow* **2004**, *30*, 1071–1091.
(16) Buffone, C.; Sefiane, K.; Christy, J. R. E. *Appl. Therm. Eng.* **2004**, *24*, 1157–1170.
(17) Buffone, C.; Sefiane, K.; Christy, J. R. E. *Phys. Fluids* **2005**, *17*, 052104.
(18) Dhavaleswarapu, H. K.; Chamarthy, P.; Garimella, S. V.; Murthy, J. Y. *Phys. Fluids* **2007**, *19*, 082103.
(19) Wang, H.; Murthy, J. Y.; Garimella, S. V. *Int. J. Heat Mass Transfer* **2008**, *51*, 3007–3017.
(20) Wee, S. K.; Kihm, K. D.; Hallinan, K. P. *Int. J. Heat Mass Transfer* **2005**, *48*, 265–278.
(21) Schrage, R. W. *A theoretical study of interphase mass transfer*; Columbia University Press: New York, 1953.
(22) Skinner, L. M.; Sambles, J. R. *J. Aerosol Sci.* **1972**, *3*, 199–210.
(23) Fisher, L. R. *Adv. Colloid Interface Sci.* **1982**, *16*, 117–125.

(24) Fisher, L. R.; Gamble, R. A.; Middlehurst, J. *Nature* **1981**, *290*, 575–576.

(25) Fisher, L. R.; Israelachvili, J. N. *J. Colloid Interface Sci.* **1981**, *80*, 528–541.

(26) DasGupta, S.; Schonberg, J. A.; Wayner, P. C. *ASME Trans. J. Heat Transfer* **1993**, 115.

(27) Swanson, L. W.; Herdt, G. C. *ASME Trans. J. Heat Transfer* **1992**, 114.

(28) Aoki, K.; Cercignani, C. *Phys. Fluids* **1983**, *26*, 1163–1164.

(29) Philip, J. R. *J. Chem. Phys.* **1977**, *66*, 5069.

(30) Derjaguin, B. V.; Churaev, N. V. *J. Colloid Interface Sci.* **1974**, *49*, 249–255.

(31) Langmuir, I. *Science* **1938**, *88*, 430–432.

(32) Kumar, D.; Biswas, S. K. *J. Colloid Interface Sci. 348*, 255-264.

(33) Cohan, L. H. *J. Am. Chem. Soc.* **1938**, *60*, 433–435.

(34) Broekhoff, J. C. P.; de Boer, J. H. *J. Catal.* **1967**, *9*, 8–14.

(35) Matsuoka, H.; Oka, K.; Yamashita, Y.; Saeki, F.; Fukui, S. *Microsyst. Technol. 17*, 983-990.

(36) Niels, R.; Mela, P.; Kramer, T.; Berenschot, J. W.; van den Berg, A. *Nano Lett.* **2003**, *3*, 1537–1540.

(37) Briggs, L. J. *J. Appl. Phys.* **1955**, *26*, 1001–1003.

(38) Debenedetti, P. G. *Metastable liquids*; Princeton University Press: Princeton, NJ, 1996.

(39) Lawson, K. W.; Lloyd, D. R. *J. Membr. Sci.* **1997**, *124*, 1–25.

(40) Schofield, R. W.; Fane, A. G.; Fell, C. J. D. *J. Membr. Sci.* **1987**, *33*, 299–313.

(41) Schofield, R. W.; Fane, A. G.; Fell, C. J. D. *J. Membr. Sci.* **1990**, *53*, 173–185.

(42) Schofield, R. W.; Fane, A. G.; Fell, C. J. D. *J. Membr. Sci.* **1990**, *53*, 159–171.

(43) Narayanan, S.; Fedorov, A. G.; Joshi, Y. K. *J. Micromech. Microeng.* **2010**, *20*, 10.

(44) Narayanan, S.; Fedorov, A. G.; Joshi, Y. K. *Nanoscale Microscale Thermophys. Eng.* **2009**, *13*, 30–53.